Supporting Information

One-Step Decomposition Pathway for Solution-Derived Metal Oxide Layers Driven by Hydroxyl Radical Atmospheres

*Y.A. Rivas,[1] M. Echaniz-Cintora,[1] A. Barreto,[1,4] J.A. Molina-Calzada,[2,3] J.A. Vidal-Moya,[5] M.C. Serrano,[1] R. Jiménez,[1] Í. Bretos,[1] M.L. Calzada[1]**

[1] Instituto de Ciencia de Materiales de Madrid (ICMM), CSIC, C/ Sor Juana Inés de la Cruz, 3, 28049, Madrid (Spain),

[2] Centro de Astrobiología, CSIC-INTA, Campus ESAC, Camino bajo del castillo s/n, E-28692 Villanueva de la Cañada, Madrid, Spain.

[3] Dpt. Física de la Tierra y Astrofísica. Facultad de Ciencias Físicas. Universidad Complutense de Madrid (UCM), E-28040 Madrid, Spain

[4] Facultad de Ciencias. Universidad Autónoma de Madrid (UAM). Ciudad Universitaria de Cantoblanco. E-28049 Madrid, Spain.

[5] Instituto de Tecnología Química (UPV-CSIC), Universitat Politécnica de Valencia – Consejo Superior de Investigaciones Científicas. E-46022, Valencia, Spain.

1. SYNTHESIS OF THE PRECURSOR SOLUTION AND DEPOSITION OF FILMS

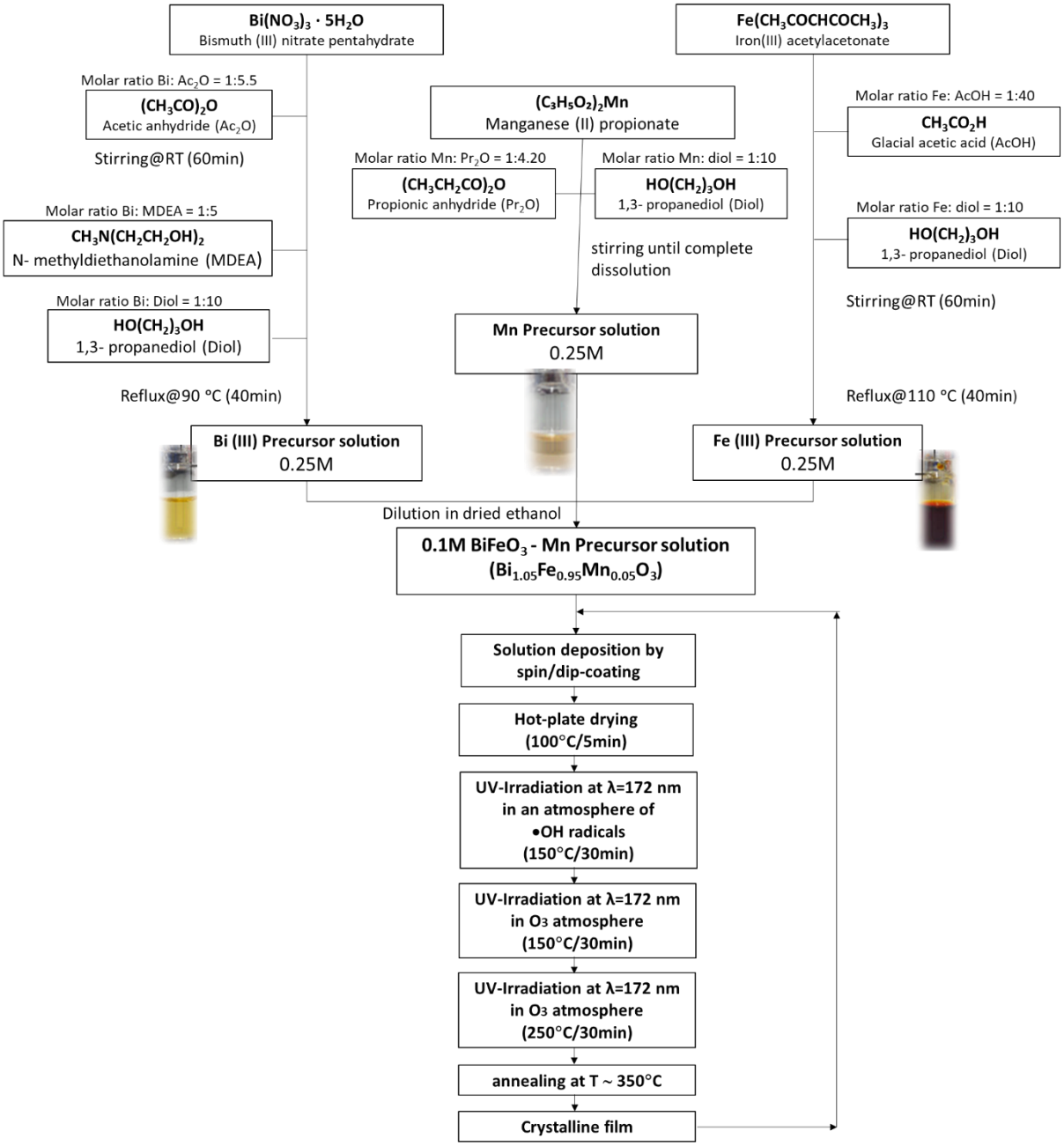

Figure S1. Scheme of the low-temperature solution deposition process of $BiFeO_3$ perovskite thin films by using the UV-irradiation of the films with an excimer lamp of λ = 172 nm in photogenerated atmosphere of •OH free radicals for accelerating the formation of the metal oxide film. The synthesis of the $BiFeO_3$ precursor solutions is shown at the top of the diagram whereas the solution-based film deposition, UV irradiation, and thermal crystallization treatment are shown at the bottom.[1-3]

The broad applicability of the hydroxyl radical–assisted fabrication process shown in **Figure S1** was tested not only for bismuth ferrite ($BiFeO_3$) perovskite films, but also across a wide range of metal oxide compositions, from binary oxides (TiO_2, Bi_2O_3) to quaternary oxides ($PbZr_{0.3}Ti_{0.7}O_3$), using different metal precursors and solution chemistries.

It is important to note that the TiO_2 films were deposited from precursor solutions containing a modified titanium alkoxide, specifically titanium diisopropoxide bis-acetylacetonate ($Ti(OCH(CH_3)_2)_2(CH_3COCHCOCH_3)_2$). The Bi_2O_3 films were prepared from precursor solutions containing the Bi–*mdea* complex. For the PZT films, the precursor solutions were formulated using lead acetate trihydrate ($Pb(CH_3COO)_2.3H_2O$) as the lead source, zirconium tetraisopropoxide ($Zr(OCH(CH_3)_2)_4$) partially stabilized with acetylacetone ($CH_3COCH_2COCH_2$) as the zirconium source, and titanium diisopropoxide bis-acetylacetonate as the titanium source.

This is particularly significant as it underscores the broad applicability of this processing method to a wide variety of metal oxide compositions, regardless of the specific metal precursor and the chemistry of the solution used.

2. HYDROXYL (•OH) RADICAL ATMOSPHERE–DRIVEN ONE-STEP DECOMPOSITION PATHWAY FOR SOLUTION-DERIVED CRYSTALLINE METAL OXIDE FILMS

Fourier Transform Infrared Spectroscopy (FTIR) was used to preliminarily investigate the effect of different processing atmospheres — namely, a conventional O_2 atmosphere used in solution-based film processing and a less commonly employed O_2 + H_2O vapor atmosphere — with and without UV irradiation of freshly solution-deposited films on bare Si substrates. **Figure S2** shows the evolution of the integrated FTIR peak areas of the resulting films in the spectral region between 1800 and 1200 cm^{-1}, where bands associated with the main organic compounds are observed. The results clearly demonstrate the enhanced effectiveness of an atmosphere enriched in hydroxyl (•OH) radicals for the removal of organic compounds. These radicals are generated inside the reactor during film processing by UV irradiation of a H_2O vapor–saturated atmosphere, as described in the Methods section of the main manuscript. Based on these findings, a hydroxyl free-radical–assisted method for accelerating the formation and crystallization of solution-processed functional metal oxide thin films was developed, as illustrated in **Figure S3**.

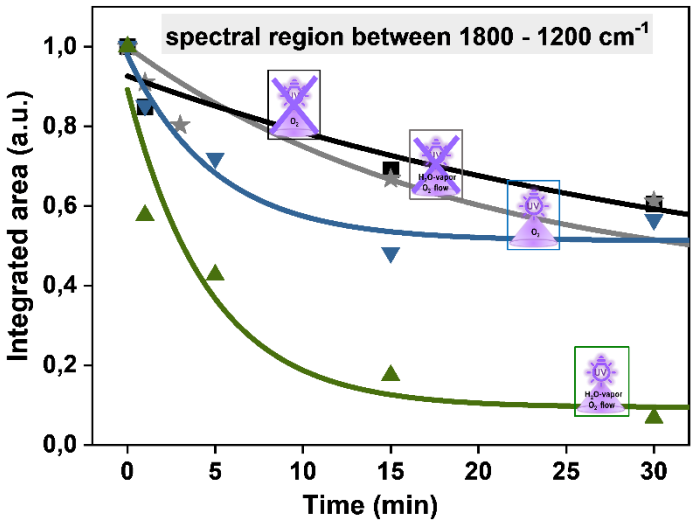

Figure S2. Time evolution of the integrated FTIR peak areas in the spectral region between 1800 and 1200 cm^{-1}, where bands associated with the main organic compounds are observed, for solution-deposited films processed under different atmospheres: a conventional O_2 atmosphere and a less commonly used O_2 + H_2O vapor atmosphere, with and without UV irradiation.[4]

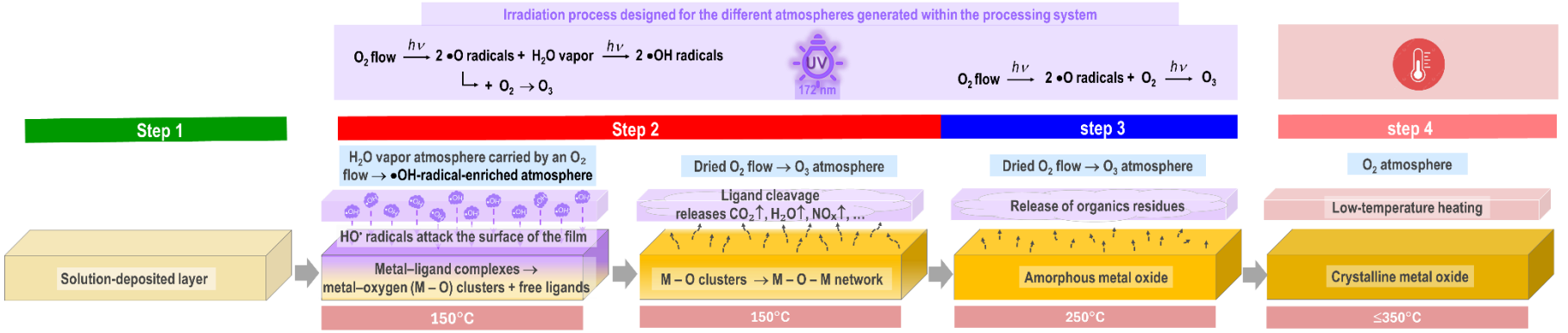

a)

Figure S3a. Continuous irradiation process developed for the hydroxyl free radical method, designed to accelerate the formation and crystallization of solution-processed functional metal oxide thin films, while operating under atmospheres generated within the processing system. The scheme illustrates the successive steps of the method: (*Step 1*) solution deposition of the film onto the substrate; (*Step 2*) treatment of the film in a •OH radical atmosphere; (*Step 3*) treatment of the film in an O_3 atmosphere; and (*Step 4*) low-temperature thermal treatment to obtain the crystalline film. The drawings representing the characteristics of the films obtained after the different steps of the devised process are shown at the bottom.[1] Detailed temperatures and soaking times used in the *Steps 2* and *3* are indicated in Figure S1.

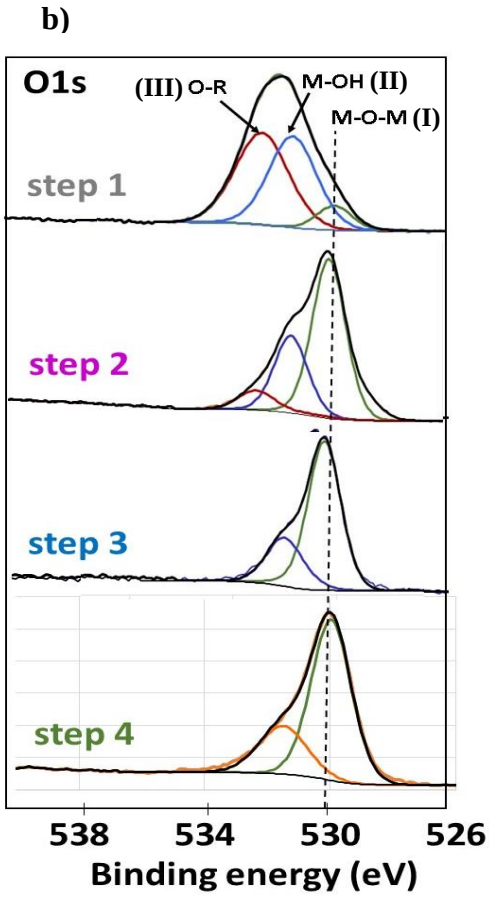

Figure S3b. O1s core level X-ray photoelectron spectroscopy (XPS) spectra for the samples after the steps 1 to 4 of the process. Experimental data here shown were acquired with a normal configuration using a tilt angle of 90º. A Shirley background was used. *Step 1*: Three components of the O1s spectrum were decomposed from an experimental peak. These components are called peaks I, II and III, from low to high binding energies. They are associated to oxygen in oxides (M – O – M compounds) (~530,1 eV), in hydroxides ($M(O–H)_x$) (~531,8 eV) and in organic compounds (O – R) (~533,1 eV), respectively. *Step 2*: A noticeable shift of the O1s spectrum to lower binding energies is observed. This O1s experimental peak can also be decomposed in three different components, also identified as peak I, II and III. *Step 3*: the experimental O1s peak can be fitted only to two peaks, I and II. *Step 4*: An experimental O1s spectrum is obtained that can also be decomposed in two peaks, I and II. The position of the peak I has now the characteristic binding energy of oxygen in oxides, with a binding energy that corresponds to that of transition metal oxides in M-O-M compounds, ~530.1 eV. The peak II is also associated to transition metal oxides. It appears as a shoulder of the main peak because it indicates the participation in the oxide of different transition metal cations. This results in metal-oxygen bonds with different binding energies, in this case Bi – O and Fe – O. Similar O1s spectra have been reported in the literature, which have been associated to transition complex metal oxides.[1]

Figure S3a schematically illustrates the four-step fabrication process designed in this work to achieve metal oxide film crystallization at low temperatures, compatible with low-cost, temperature-sensitive substrates.

These different steps involved in the gaseous •OH free-radical-assisted synthesis method designed in this work to accelerate the crystallization of metal oxide films[1] are shown in Figure S2 and can be summarized as follows:

Step 1: The precursor solutions are deposited onto the substrate, and the resulting layers are dried on a hot plate at 100 °C for five minutes.

Step 2: The films are irradiated with a UV excimer lamp (λ = 172 nm) inside a sealed chamber filled with an atmosphere saturated in water (H_2O) vapor. The vapor is introduced into the chamber via a controlled flow of O_2 gas, which transports the moisture into the irradiation environment. This UV exposure initiates photochemical reactions in the atmosphere, beginning with the photolysis of O_2 and the generation of reactive oxygen species (•O). These oxygen radicals subsequently react with H_2O vapor to produce highly reactive hydroxyl radicals (•OH), creating a radical-rich environment. Additionally, O_3 is produced as a secondary reaction due to the photolysis of residual O_2 used as the carrier gas for the H_2O vapor introduced into the sealed chamber.

Step 3: The films are further exposed to UV irradiation in an ozone-rich (O_3) atmosphere, generated by the photolysis of pure O_2 gas introduced into the sealed chamber, followed by the reaction of •O radicals with molecular oxygen.

Step 4: A furnace annealing process is applied to the films, produced in the previous processing steps, under reduced thermal load in an oxygen atmosphere outside the sealed chamber.

The subsequent treatments at *Step 4* consist in thermal treatments at temperatures ≤350ºC for different soaking times. These are referred as *Steps 5 through 11* in the next **Figure S4.**The objective is to progressively enhance the film's crystallinity at the lowest possible temperature by gradually increasing the soaking time.

In addition, Figure S3b shows the experimentally measured O1s core level X-ray photoelectron spectroscopy (XPS) spectra for the films obtained after the steps 1 to 4 of the process. The different components of the O1s XPS peak measured at each step are as follows;

Step 1: three components of the O1s spectrum were decomposed from an experimental peak. These components are called peaks I, II and III, from low to high binding energies. They are

associated to oxygen in oxides (M – O – M compounds) (~530,1 eV), in hydroxides (M(O–H)$_x$) (~531,8 eV) and in organic compounds (O – R) (~533,1 eV), respectively. *Step 2*: a noticeable shift of the O1s spectrum to lower binding energies is observed. This O1s experimental peak can also be decomposed in three different components, also identified as peak I, II and III. *Step 3*: the experimental O1s peak can be fitted only to two peaks, I and II, indicating that O – R bonds are not present in the system, and therefore all organics have been eliminated from the film at this step. *Step 4*: an experimental O1s spectrum is obtained that can also be decomposed in two peaks, I and II. The position of the peak I has now the characteristic binding energy of oxygen in oxides, with a binding energy that corresponds to that of transition metal oxides in M-O-M compounds, ~530.1 eV. The peak II is also associated to transition metal oxides. It appears as a shoulder of the main peak because it indicates the participation in the oxide of different transition metal cations. This results in metal-oxygen bonds with different binding energies, in this case Bi – O and Fe – O. Similar O1s spectra have been reported in the literature, which have been associated to transition complex metal oxides.[1]

3. SOLUTION-DERIVED METAL OXIDE FILM CRYSTALLIZATION DRIVEN BY GASEOUS •OH RADICALS

3.1. Evolution of the vibrational modes recorded by IRRAS

The integrated areas of the bands associated with the different bonds have been calculated for each processing step using the experimental data recorded in **Figure S4**. This evolution is shown in Figure S4a for the various modes: (i) ν(O – H), (ii) $\nu(C-H)_O$, $\nu(C-H)_N$, and $\nu(C-H)_{C=O}$, (iii) ν(C – O), (iv) ν(C = N), (v) ν(C = O) and ν(C – C), and (vi) ν(M – O). These calculations were performed for an annealing process, in which the film is dried and pyrolyzed in an air atmosphere (*Steps 2 and 3*), followed by annealing in oxygen (*Step 4*) (hereinafter conventional process). The same process was also analyzed using a H_2O vapor atmosphere during *Steps 2 and 3*, as well as for the process designed, which employs an atmosphere of •OH free radicals during *Steps 2 and 3*. The fitting of the IRRAS data is shown for each vibrational mode. The fitting of the curves obtained for these calculated areas, corresponding to the different vibrational modes, is also included in Figure S4a. The reaction mechanisms, such as reaction rates and the rupture and formation of bonds, can be inferred from the fitting of these curves. The curves of the different vibration modes have been adjusted using various mathematical functions, resulting in fittings with high goodness-of-fit (adj. R-Squares > 0.99). The cleavage mechanisms of the different bonds present in the chemical system, as well as the formation of metal-oxygen bonds, have been inferred for each processing method. These mechanisms are explained in relation to each graph. Additionally, a calculation of the integrated area of the peak recorded in the spectral region below 750 cm^{-1}, where the ν(M-O) band primarily appears, is shown in Figure S4b throughout the processes, finally leading to its splitting in the two bands characteristic of the crystalline $BiFeO_3$ perovskite, in the case of the process carried out under •OH-radicals atmosphere.[1]

a)

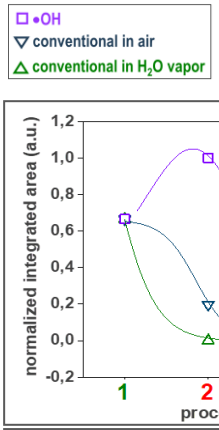

At *Step 2*, •OH radicals are intentionally UV-generated in the atmosphere where the films are processed. These radicals attack the film surface, inducing primary reactions with the $(C–H)_O$, $(C–H)_{C=O}$, and $(C–H)_N$ bonds of the metal ligands. This leads to a wide range of different intermediate organic compounds with labile O–H bonds, which are responsible for the significant increase observed in the ν(O-H) vibrational mode at *Step 2*. These O–H groups are quickly eliminated in the next step, *Step 3*, giving rise to hydrocarbon compounds that are easily removed from the system. In this case, the reaction mechanism under •OH radical atmospheres fits well to a GaussAmp function (a Gaussian curve with adjustable amplitude), showing a goodness-of-fit with adjusted R-squared values greater than 0.99. In contrast, when the processes referred to here as conventional are used, either under air or water vapor atmospheres, the O–H groups are removed

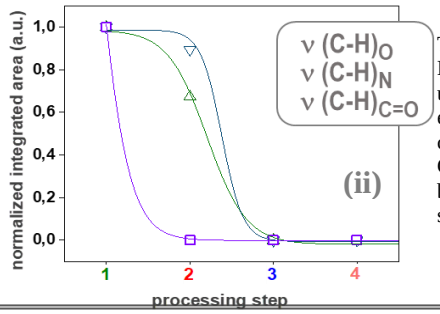

The curves corresponding to the cleavage of the C–H bonds (ν(C–H) vibrational mode) can be fitted to Boltzmann functions with a very high goodness-of-fit, adj. R-Squares > 0.99. The cleavage of these bonds under an atmosphere of •OH radicals occurs through a reaction with a very high cleavage rate. An exponential decay of the C–H bonds to zero occurs from *Step 1* to *Step 2*. However, the initiation of C–H cleavage is delayed and slow in the referred as conventional processes, both under air and water vapor, with C–H cleavage occurring more slowly under air than under water vapor. Thus, the C–H bonds are gradually broken between *Step 1* and *Step 2* in conventional processes, with total disappearance from the chemical system only after *Step 3*.

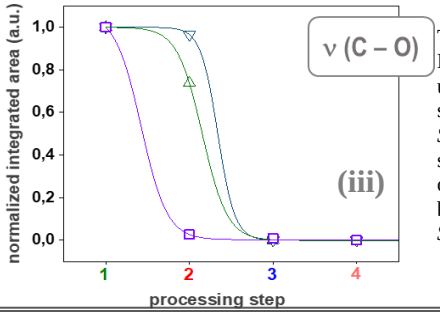

The curves corresponding to the cleavage of the C–O bonds (ν(C–O) vibrational mode) can be fitted to Boltzmann functions with a very high goodness-of-fit, adj. R-Squares > 0.99. The cleavage of these bonds under an atmosphere of •OH radicals occurs through a reaction with a very high cleavage rate, although slightly lower than that of the C–H bonds. Therefore, a strong decay of the C–O bonds to zero occurs from *Step 1* to *Step 2*. However, similar to the C–H bonds, the initiation of C–O cleavage is delayed and proceeds slowly in what are referred to as conventional processes, both under air and water vapor, with C–O cleavage occurring more slowly under air than under water vapor. Consequently, the C–O bonds are gradually broken between *Step 1* and *Step 2* in conventional processes, with total disappearance from the chemical system after *Step 3*.

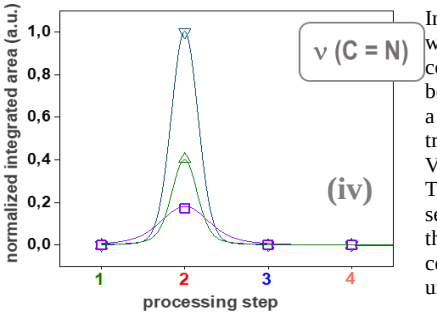

In analyzing this band, it is important to consider that methyldiethanolamine (*mdea*, the ligand in this system), which is responsible for the appearance of this band in the IR spectrum, is a tertiary amine and does not contain a C=N group in its original structure. However, upon coordination with bismuth, a partial double bond character is developed between the nitrogen and the adjacent carbon, which results in the IR spectrum as a band in the 1600–1650 cm^{-1} region, which resembles that of an imine, although it does not correspond to a true C=N bond. [5] The curves corresponding to the cleavage of the C=N bonds can be accurately fitted using Voigt functions, showing a very high goodness-of-fit (adjusted $R^2 > 0.99$), with maxima occurring at *Step 2*. This suggests that these bonds, which are present in the Bi-*mdea* complex, break at this stage, triggering secondary reactions that lead to the formation of intermediate compounds with amine groups. As shown in this figure, the intensity of the C=N bonds reaches a minimum maximum at *Step 2* under an atmosphere containing •OH radicals. This indicates that the formation of these compounds with amine groups is hindered under an atmosphere of •OH radicals. In all processes, these C=N bonds completely disappear after *Step 3*.

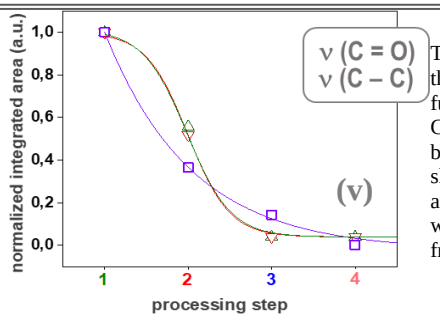

The C–C and C=O bonds (ν(C–C) and ν(C=O) vibrational modes) seem to be the last bonds cleaved during the various processing methods studied here. In all cases, the cleavage curves can be fitted to Boltzmann functions, with a very high goodness-of-fit, adj. R-Squares > 0.99. It should be noted that the cleavage of the C–C and C=O bonds occurs quickly and follows a similar pathway in the referred as conventional processes, both in air and water vapor. In processes involving atmospheres of •OH radicals, these bonds break more slowly than in the former. However, the continuous elimination of CO_2 observed in Figures S6a and S6b, well after *Step 3*, indicates the presence of organic residues in the subsequent steps of the conventional processes, which use extended thermal budgets at 350 ºC. This is detrimental to the formation of an amorphous, defect-free, high-density metal-oxygen network.

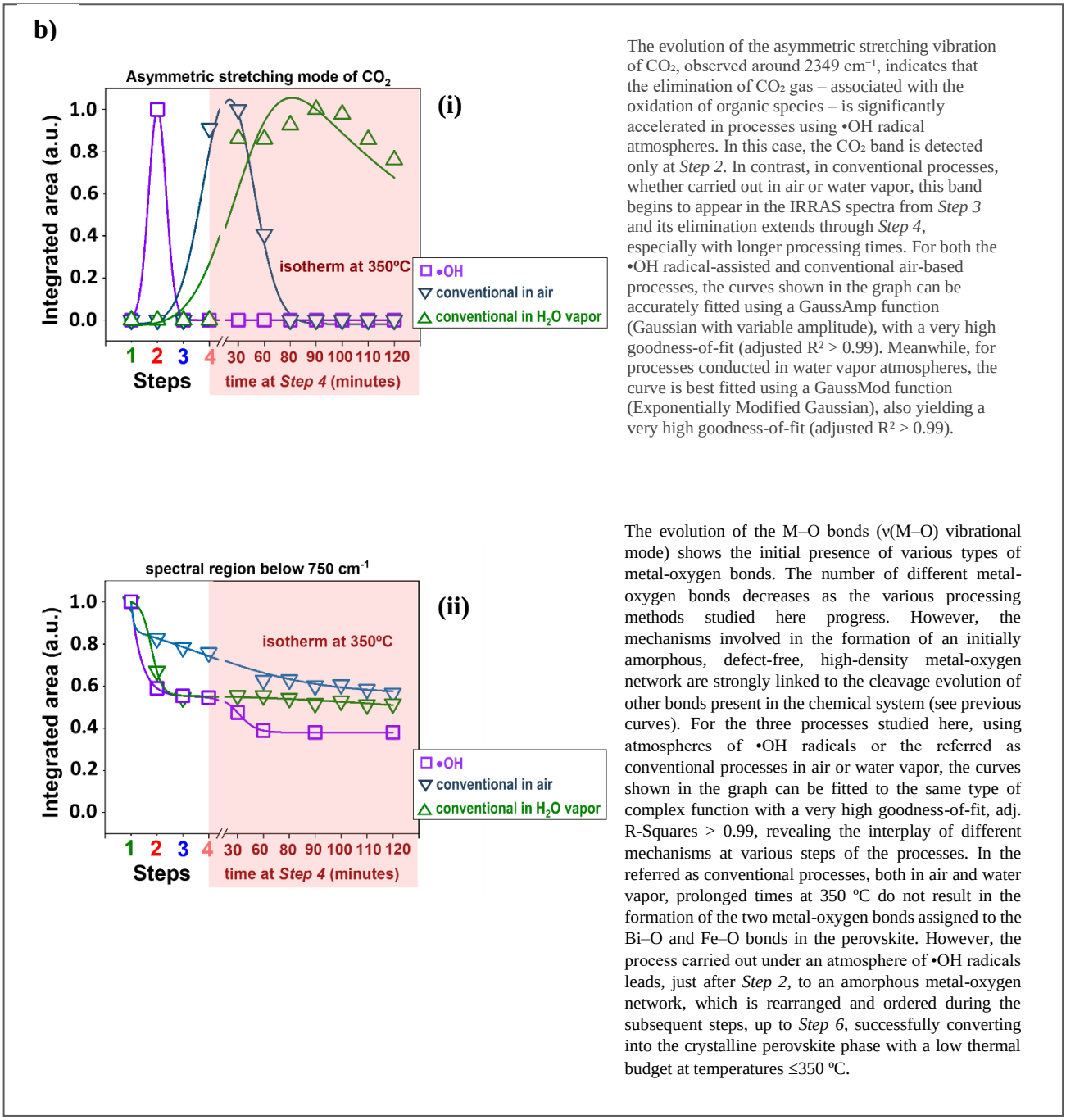

Figure S4. a) Calculated integrated areas of the different vibrational modes recorded through IRRAS analysis for the film at various stages of the solution deposition process aided by an atmosphere of •OH radicals, compared to those calculated for the film processed through the as referred as conventional solution deposition methods carried out in a H_2O vapor atmosphere and in an air atmosphere. The fitting of the IRRAS data is shown for each vibrational mode. Note that the normalization of the integrated areas corresponding to the ν(O-H) and ν(C=N) bonds was performed using the maximum value calculated in *Step 2* of the •OH-radical-assisted and conventional process, respectively. The continuous violet, red, and green lines correspond to the fitting curves of the IRRAS data. **b)** (i) Calculated area of the asymmetrical vibrational mode recorded at 2349 cm^{-1} assigned to CO_2 and (ii) calculated rea of the broad band recorded in the spectral region below 750 cm^{-1}, where the ν(M–O) band primarily appears. These areas have been calculated from the IRRAS spectra of the films at each stage of the •OH-assisted solution deposition process, as well as at each stage of the conventional solution deposition process carried out in air in water vapor.

3.2. Study of the Metal–Nitrogen Bonds by FTIR

Fourier Transform Infrared Spectroscopy (FTIR) was employed to investigate the wavelength range in which metal–nitrogen bonds are typically detected (below 200 cm^{-1}). Measurements were performed using a Bruker IFS 66V-S spectrometer over the wavelength range of 1000 cm^{-1} to 50 cm^{-1}, exclusively for the bismuth precursor. This approach allows differentiation between the Bi–N bond, which appears between 50 cm^{-1} and 200 cm^{-1}, and the Bi–O bond, which appears between 200 cm^{-1} and 1000 cm^{-1}.

Directly deposited films on substrates were not suitable for this analysis due to interference from the substrate. Therefore, FTIR measurements were performed on pellets prepared from the gel bismuth precursor samples obtained after treatment in the sealed chamber (Figure S2), mixed with polyethylene $(C_2H_4)_n$, which does not absorb in this spectral region.

Gel samples were prepared by placing 300 µL of the solution into a flat alumina crucible to maximize the surface area exposed to the reactive atmosphere. The crucible was then placed in a sealed chamber and subjected to the various processing conditions investigated in this study.

4. ELECTRON PARAMAGNETIC RESONANCE (EPR) MEASUREMENTS

Electron Paramagnetic Resonance (EPR) is a powerful spectroscopic technique used to study materials containing unpaired electrons, such as free radicals. It detects the resonance absorption of microwave radiation by unpaired electrons in the presence of a magnetic field.

In this study, EPR was employed in an unconventional manner: rather than analyzing radicals in solution, the technique was used to investigate the formation of an atmosphere enriched in gaseous hydroxyl radicals (•OH). This was achieved by introducing water vapor (H_2O) into a sealed chamber and irradiating it with a UV excimer lamp at a wavelength of 172 nm.

EPR spectra were recorded at room temperature (RT) with a Bruker EMX-12 spectrometer operating at the X-band, with a modulation frequency of 100 kHz and an amplitude of 0.1 mT.

Figure S5 presents the EPR spectra obtained from experiments using two different spin-trapping agents: 2,2,6,6-Tetramethylpiperidine 1-oxyl (TEMPO) and 5,5-Dimethyl-1-pyrroline N-oxide (DMPO). These agents were introduced into the hermetically sealed chamber, which was saturated with water vapor and subjected to UV irradiation. For sample preparation, 300 μL of aqueous or ethanol-dried solutions of TEMPO or DMPO were placed in flat alumina crucibles to maximize the surface area exposed to the surrounding reactive atmosphere.

The samples were diluited in deionized water and dried ethanol-for EPR measurement. These experiments were specifically designed to confirm the formation of an •OH radical-enriched atmosphere during *Step 2*, when water vapor in the sealed chamber is irradiated with 172 nm UV light from the excimer lamp.

The corresponding EPR spectra are shown in Figure S5.

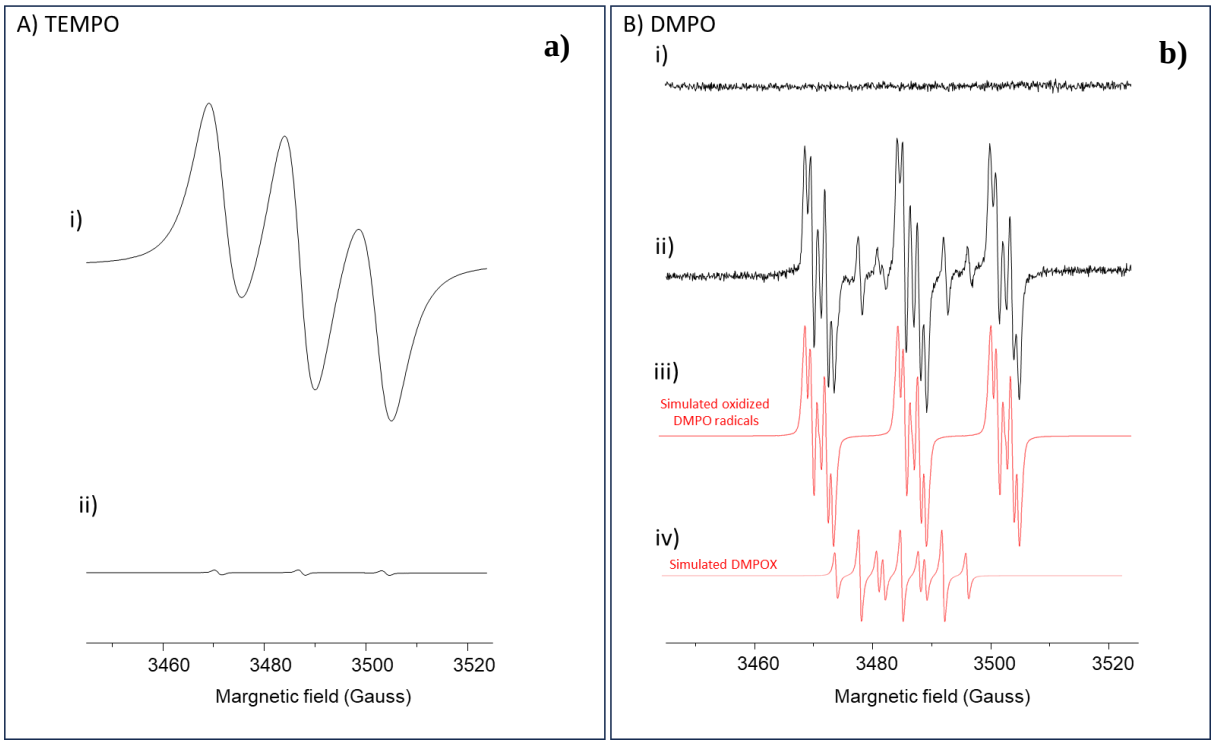

Figure S5. Electro Paramagnetic Resonance (EPR) spectra of **a)** TEMPO solution (0.1 mol/L), corresponding (i) to this solution without any treatment and (ii) to this solution treated at room temperature for 30 min under an atmosphere enriched in •OH radicals. **b)** Spectra of the DMPO solution (0.65 mol/L), corresponding (i) to this solution without any treatment, (ii) to this solution treated at room temperature for 30 min under an atmosphere enriched in •OH radicals, (iii) and (iv) represent the simulated spectra for the spectrum of DMPO shown in (ii). The EPR parameters used for these simulation are as follow: a_N = 15.65 G and $a_{\gamma H}$ = 1.43 G (3H) for HDMPO-OH, and a_N = 7.1 G and $a_{\gamma H}$ = 4.2 G (2H) for DMPOX.

Figure S5a displays the electron spin resonance (EPR) spectra obtained from an aqueous-dried ethanol solution of TEMPO (0.10 mol/L), both before (i), control sample, and after (ii) exposure to an atmosphere enriched with hydroxyl radicals (•OH) for 30 minutes at room temperature. The spectrum of the control sample (i) shows a strong and characteristic TEMPO signal, consisting of a well-defined triplet pattern attributed to the hyperfine interaction between the unpaired electron and the nitrogen nucleus.

In contrast, the spectrum of the sample exposed to •OH radicals (ii) reveals an almost complete disappearance of the EPR signal. This suggests that TEMPO reacts with the reactive species generated during irradiation, presumably hydroxyl radicals, forming EPR-silent products that are undetectable by this technique.

Figure S5b presents the EPR spectra of an aqueous-dried ethanol solution of DMPO (0.65 mol/L), recorded before (i) and after (ii) 30 minutes of exposure to the •OH -enriched atmosphere. Simulated spectra obtained are shown in (iii) and (iv), corresponding to: the DMPOX adduct (oxidation product of DMPO), characterized by hyperfine coupling constants of a_N = 7.1 G and a_H = 4.2 G (2H), and degradation product of the •OH–DMPO adduct, with coupling constants a_N = 15.65 G and a_H = 0.78 G, 1.11 G, and 2.39 G.

These results provide indirect evidence for the generation of hydroxyl radicals (•OH) in the processing atmosphere of the solution-deposited films.[6-8] This atmosphere is created during UV irradiation using a 172 nm excimer lamp in a sealed chamber filled with water vapor, which is generated by passing pure oxygen through distilled water before introducing it into the chamber, as detailed in the Experimental Section.

5. FUNCTIONAL PROPERTIES OF SOLUTION-DERIVED $BiFeO_3$ FILMS:

CONVENTIONAL (500 °C) *vs* •OH-ASSISTED ATMOSPHERE PROCESSING (350 °C)

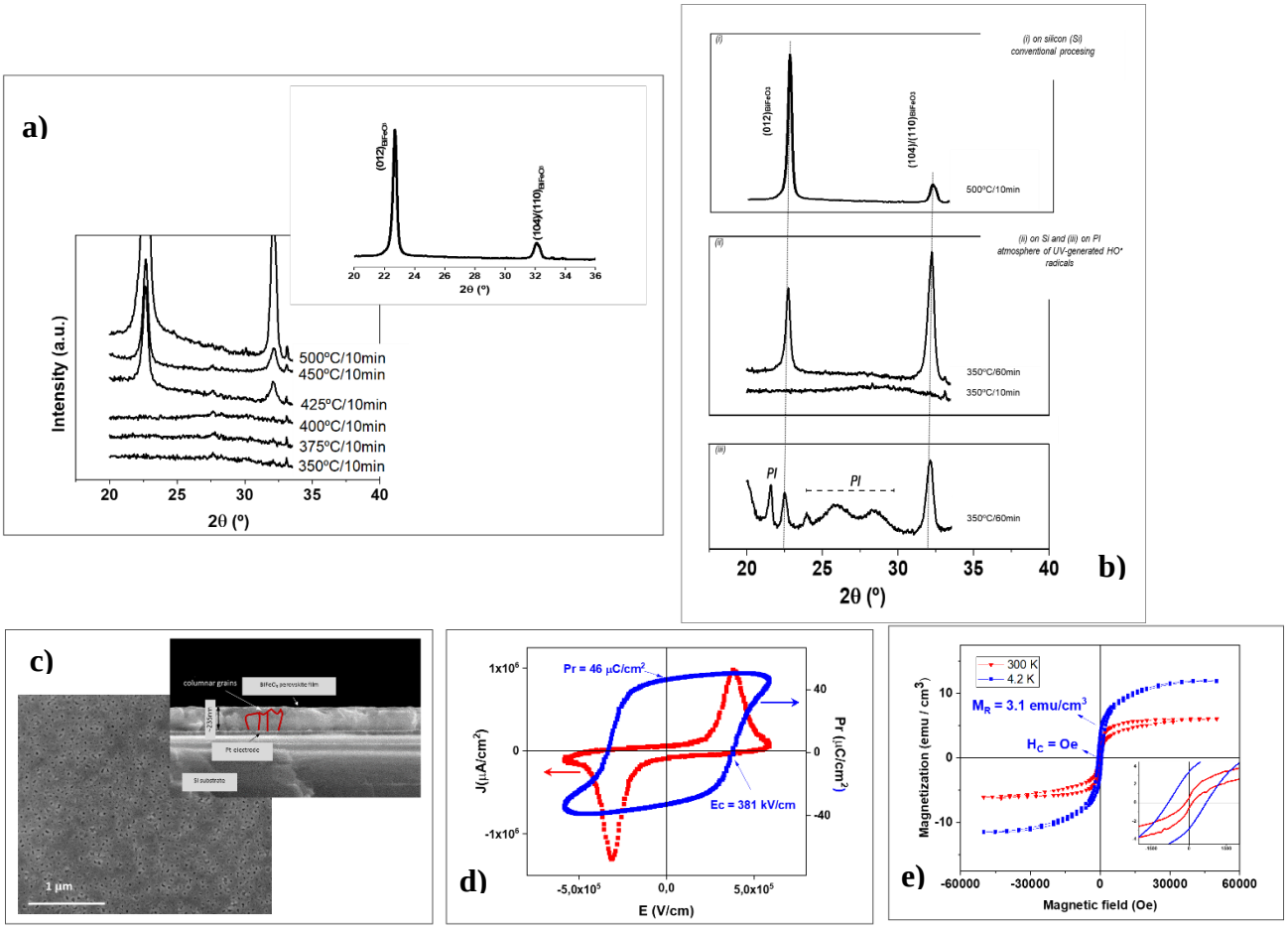

Figure S6. Functional properties of the $BiFeO_3$ films conventionally processed at high temperatures (500ºC). **a)** X-ray diffraction (XRD) patterns of the films conventionally processed at different temperatures, to determine when the perovskite phase is detected in the patters. The XRD patterns show that the perovskite films grow with a preferred orientation along the <012> axis of the rhombohedral phase structure.[3] **b)** XRD patterns of the $BiFeO_3$ films deposited on (i) Pt-coated (100)Si substrates by a conventional processed and crystallized at high temperature (500ºC). These films show a preferred orientation along the (012) axis of the perovkite. For comparison (ii) and (iii) show the $BiFeO_3$ films deposited at a low temperature (350ºC) on Pt-coated Si substrates and flexible Polyimide (PI). These films show a random orientation of the perovskite. **c)** Scanning Electron Microscopy (SEM) images of the surface and cross-section of the $BiFeO_3$ thin film fabricated by a conventional solution deposition process at a high temperature of 500ºC. In the cross-sectional image, a schematic representation of the columnar grain growth observed in the high-temperature processed films is shown. This type of microstructure is responsible for the strong ferroelectric switching exhibited by these films, resulting in high remnant polarization (P_R) values. **d)** Ferroelectric (P-E) hysteresis loop and current vs applied field (J-E) curve measured in this film. Remnant polarizations of $P_R \sim 46\ \mu C/cm^2$ and coercive fields of $E_C \sim 381$ kV/cm, are measured from this loop. **e)** Magnetization *vs*. Magnetic field (M – H) loops, measured at room temperature (@RT, 300 K) and low temperature (4.2 K), in these films on Pt-coated Si substrates and conventionally processed at 500ºC.

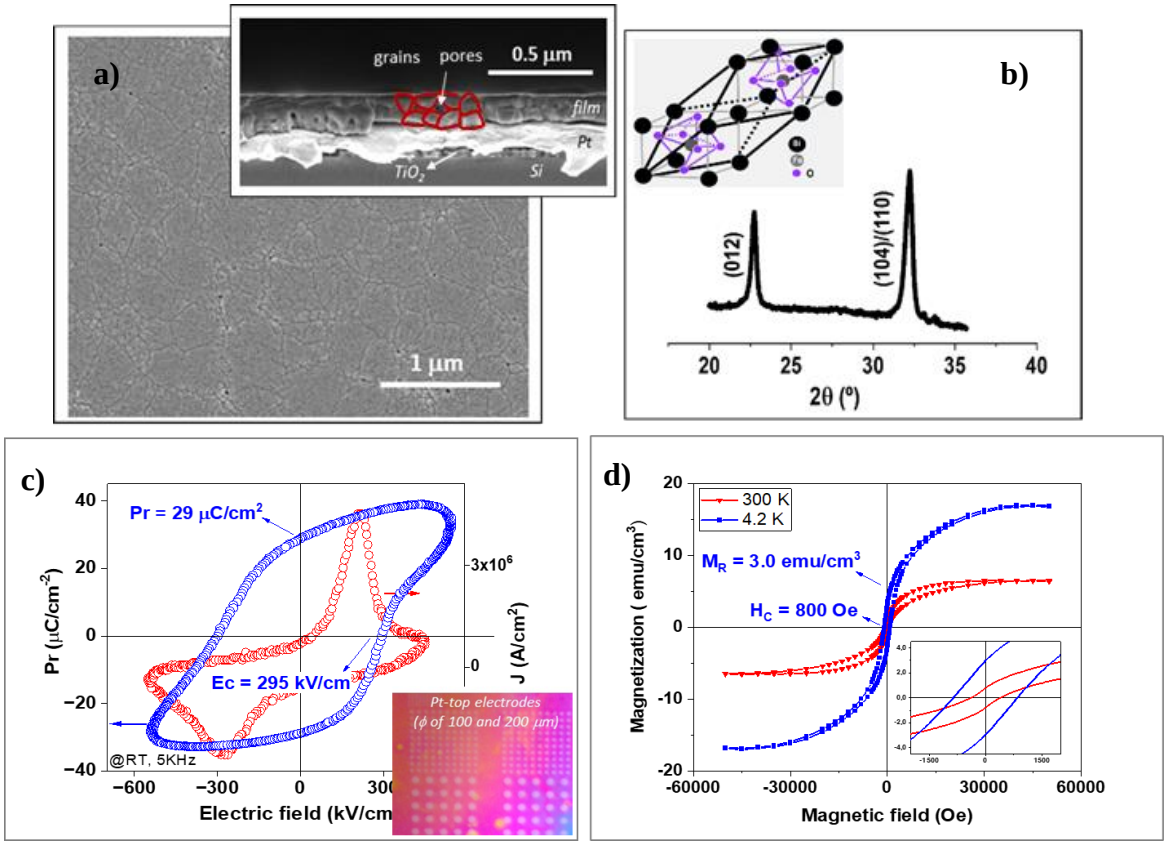

Figure S7. Functional properties of the $BiFeO_3$ films deposited on Pt-coated Si substrates processed under a low thermal budget at 350ºC, using atmospheres enriched with •OH radicals. **a)** SEM surface and cross-sectional images of the $BiFeO_3$ films. In the cross-sectional image, a schematic representation of the polycrystalline grain growth with intergranular porosity observed in this low-temperature processed films is shown. This intergranular porosity, oriented perpendicular to the applied electric field, disrupts ferroelectric switching during poling. This interruption prevents efficient poling due to the lack of continuous ferroelectric pathways. As a result, because ferroelectricity is inherently cooperative, not all regions of the ferroelectric phase can respond to the applied field, leading to the lower P_R value observed in the low-temperature processed film compared to the high-temperature processed one. **b)** XRD pattern of the perovskite film, accompanied by a schematic of the rhombohedral $BiFeO_3$ crystal structure. The diffraction peaks in the XRD pattern are indexed according to JCPDS Card No. 86-1518. **c)** Ferroelectric hysteresis loop (P–E) and current density *vs.* electric field (J–E) curves measured at room temperature (@RT) for the $BiFeO_3$ film deposited on Pt-coated (100)Si substrates. The inset displays a photograph of the film and the array of capacitors fabricated for electrical characterization. **d)** Magnetization *vs.* Magnetic field (M – H) loops, measured at room temperature (@RT, 300 K) and at low temperature (4.2 K).

Therefore, by employing the •OH radical-assisted atmosphere fabrication process, $BiFeO_3$ perovskite thin films can be obtained using a low thermal budget (at 350 °C/60 min). **Figure S7** shows the properties of these films prepared on Pt-coated (100)Si substrates. As observed, they exhibit a polycrystalline microstructure consisting of nanosized, rounded grains with integranular porosity (**Figure S7a**). No regions indicating phase contrast were observed, suggesting the absence of secondary or non-perovskite phases. In contrast to conventionally

processed films at high temperatures (**Figure S6**), the films fabricated at 350 °C do not exhibit columnar growth in cross-sectional views. This behavior is consistent with the random orientation observed in their XRD patterns (Figure S7b), attributed to the homogeneous nucleation of the perovskite phase throughout the film and subsequent grain growth during low-temperature annealing.

A representative ferroelectric hysteresis loop of this sample is shown in Figure S7c. Over 90% of the capacitors (see inset) exhibited appropriate permittivity values and low dielectric losses.[3]. A remnant polarization (P_R) of approximately 29 μC/cm² and a coercive field (E_C) of ~ 295 kV/cm were obtained at room temperature. As expected, this P_R value is lower with respect to $BiFeO_3$ thin films processed at higher temperatures (Figure S6) due to the widely reported reduction of ferroelectric performance at the nanoscale in low-temperature processed samples, but also to the intergranular porosity present in the low-temperature processed film, oriented perpendicular to the applied electric field, that disrupts ferroelectric switching during poling. This interruption prevents efficient poling due to the lack of continuous ferroelectric pathways. As a result, because ferroelectricity is inherently cooperative, not all regions of the ferroelectric phase can respond to the applied field, leading to the lower P_R value observed in the low-temperature processed film compared to the high-temperature processed one. Nevertheless, the P_R value achieved significantly exceeds the requirements for a potential application in ferroelectric devices and compares favorably with most low-temperature-processable ferroelectrics (particularly organic ones).

The most compelling demonstration of the effectiveness of this processing method is the successful crystallization of the complex ferroelectric perovskite $Pb(Zr_{0.30}Ti_{0.70})O_3$ (PZT), a solid solution of three oxides (PbO, TiO_2, and ZrO_2), and even more complex than the $BiFeO_3$ system (a solid solution of two oxides: Bi_2O_3 and Fe_2O_3) (**Figure S8**). XRD analysis confirms the formation of the crystalline perovskite PZT phase at an annealing temperature of only 350 °C. Furthermore, the films exhibit well-defined ferroelectric behavior, as evidenced by

the measured hysteresis loops from capacitors fabricated on these films. These devices show a remanent polarization (P_R) of approximately 14 μC/cm² and a coercive field (E_C) of around 340 kV/cm (Figure 9b). These results provide compelling evidence of the high quality of the films produced using this method and underscore its potential for the fabrication of functional oxide-based devices at significantly reduced thermal budgets.

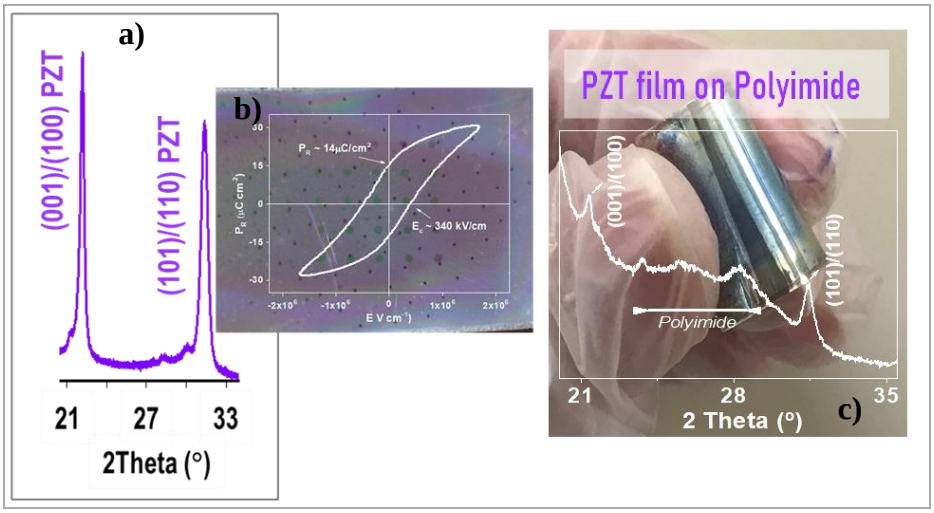

Figure S8. **a)** XRD pattern of a $Pb(Zr_{0.30}Ti_{0.70})O_3$ (PZT) thin film processed under an •OH radical-enriched atmosphere and annealed at only 350 °C. The diffraction peaks have been indexed according to JCPDS-ICDD Card No. 01-070-4055 for the PZT perovskite phase. **b)** Ferroelectric hysteresis loop measured from this film, along with a photograph of the sample displaying the array of capacitors fabricated for electrical characterization. **c)** Photograph of a flexible PZT film directly deposited on a PI substrate, accompanied by the corresponding XRD pattern of the film.

6. *GENERAL APPLICABILITY OF THE METAL OXIDE SOLUTION SYNTHESIS PLATFORM*

6.1 Reduction of the activation energy (Ea) for the crystallization of metal oxide films. The case of single TiO_2 oxide films

TiO_2 (anatase) thin films were deposited from precursor solutions with a titanium oxide concentration equivalent to 0.3 mol/L. These solutions were prepared by diluting titanium diisopropoxide bis(acetylacetonate) ($[Ti(OCH(CH_3)_2)_2(C_5H_7O_2)_2]$, 75 wt% in isopropanol, Sigma-Aldrich-Merck) in absolute ethanol (C_2H_5OH, Sigma-Aldrich-Merck). The resulting solutions were spin-coated onto Pt-coated Si substrates at 2000 rpm for 45 seconds.

The wet films were initially dried on a hot plate at 100 °C for 5 minutes. Subsequently, they were subjected to the processing methods devised in this work: the referred as conventional processing in air, and that involving exposure to an atmosphere rich in hydroxyl (•OH) radicals generated via UV irradiation. Then, annealing was performed in an oxygen atmosphere at temperatures ranging from 200 °C to 600 °C, with soaking times varying between 10 minutes and 5 hours. X-ray diffraction (XRD) patterns were recorded for each condition, and the area of the (101) anatase TiO_2 peak was quantified.

From these data, Avrami plots were determined to analyze the crystallization kinetics. The crystallization rate constants derived from these plots were used to generate Arrhenius plots, enabling the determination of the activation energy (Ea) for anatase phase crystallization under each processing condition (**Figure S9**).

Figure S9a illustrates that incipient crystallization of TiO_2 occurs at an extremely low thermal budget, 250 °C for 180 minutes, when processed in the presence of •OH radicals. In contrast, films processed conventionally in air remain amorphous under the same conditions, showing no evidence of anatase phase formation.

Activation energies calculated from the Arrhenius plots (Figure S9b) reveal two key findings. First and foremost, the activation energy (E_a) for crystallization is lower for films treated in

the •OH radical atmosphere compared to those processed conventionally – approximately 490 kJ/mol and 750 kJ/mol, respectively – in the low-temperature regime (below ~350 °C). However, in the high-temperature regime, the E_a values calculated for both fabrication processes are essentially the same, indicating that above 350 °C the energy barrier for crystallization of the metal oxide phase has already been overcome, and the influence of the processing atmosphere becomes negligible.

These findings demonstrate that the presence of highly reactive •OH radicals significantly accelerates the crystallization of solution-deposited TiO_2 films, enabling lower-temperature processing and potentially enhancing the efficiency of this fabrication method for functional oxide materials.

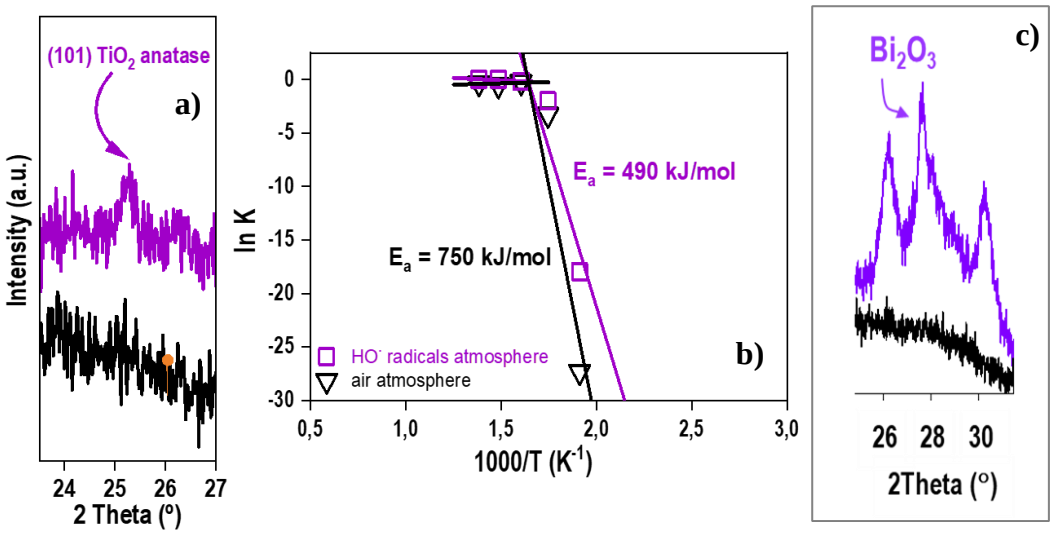

Figure S9. a) X-ray diffraction (XRD) patterns in the 2θ range highlighting the main (101) reflection of anatase TiO_2, recorded for films processed conventionally in air and those fabricated under an atmosphere enriched with hydroxyl (•OH) radicals. The diffraction peaks have been indexed according to the JCPDS Card No. 21-1272 for anatase TiO_2. **b)** Arrhenius plots of the crystallization rate constant (K) versus inverse temperature (1/T) for the same two sets of films, illustrating the enhanced crystallization kinetics under •OH radical-rich conditions. **c)** X-ray diffraction (XRD) patterns in the 2θ range highlighting the main reflections of Bi_2O_3: the (120) peak of α-Bi_2O_3 (JCPDS Card No. 41-1449), the (111) peak of δ-Bi_2O_3 (JCPDS Card No. 27-0050), and the (201) peak of β-Bi_2O_3 (JCPDS Card No. 78-179). These characteristic peaks are absent in films processed conventionally in air at 250ºC but are clearly observed in those fabricated under an atmosphere enriched with hydroxyl (•OH) radicals and annealed at 250ºC.

This kinetic study demonstrates that the crystallization of TiO_2 films using the gaseous •OH radical–assisted processing platform initiates at lower temperatures than those required for

more structurally complex ferroelectric oxides, such as the $BiFeO_3$ films used here as a proof of concept, or the PZT perovskite films (Figures S7 and S8). This behavior is primarily due to the greater structural complexity of these multicomponent oxides. The formation of a well-ordered perovskite structure in $BiFeO_3$ or PZT requires more intricate atomic rearrangements and stricter stoichiometric control, which generally demand higher thermal energy to trigger crystallization.

Similarly to the TiO_2 films, a comparable behavior is observed for another single-component oxide, Bi_2O_3, which exhibits multiple polymorphic forms, many of them metastable at room temperature. When processed using the hydroxyl (•OH) radical–enriched solution film platform, Bi_2O_3 films begin to crystallize at temperatures as low as 250 °C, forming a mixture of structural phases (Figure S9c). By contrast, films processed conventionally in air remain amorphous under the same annealing conditions.

It is important to note that the TiO_2 films were deposited from precursor solutions containing a modified titanium alkoxide, specifically titanium diisopropoxide bis-acetylacetonate ($Ti(OCH(CH_3)_2)_2(CH_3COCHCOCH_3)_2$). The Bi_2O_3 films were prepared from precursor solutions containing the Bi–*mdea* complex, as previously described in this work. For the PZT films, the precursor solutions were formulated using lead acetate trihydrate ($Pb(CH_3COO)_2.3H_2O$) as the lead source, zirconium tetraisopropoxide ($Zr(OCH(CH_3)_2)_4$) partially stabilized with acetylacetone ($CH_3COCH_2COCH_2$) as the zirconium source, and titanium diisopropoxide bis-acetylacetonate as the titanium source.

This is particularly significant, as it underscores the broad applicability of this processing method to a wide variety of metal oxide films, irrespective of the specific metal-organic, metal alkoxide or metal salt reagents employed in the synthesis of the precursor solutions used in the CSD deposition of films. The method demonstrates robust performance across diverse solution chemistries, highlighting its versatility for the fabrication of high-quality oxide films from various precursor formulations.

REFERENCES

1. A.Gómez-Lopez, Y.A.Rivas, S.López-Fajardo, R.Jiménez, J.Ricote, C.Pecharromán, I.Montero, I.Bretos, M.L.Calzada. *In situ* photogenerated hydroxyl radicals in the reaction atmosphere for the accelerated crystallization of solution-processed functional metal oxide thin films. *J. Mater. Chem. C*, **2023**, *11*, 2619-2629.

2. D. Pérez-Mezcua, R.Sirera, R.Jiménez, I.Bretos, C.De Dobbelaere, A.Hardy, M.K.Van Bael, M.L.Calzada. A UV-absorber bismuth(III)-N-methyldiethanolamine complex as a low temperature precursor for bismuth-based oxide thin films. *J. Mater. Chem. C*, **2014**, *2*, 8750–8760.

3. C.Gutierrez-Lazaro, I.Bretos, R.Jimenez, J.Ricote, H.El Hosiny, D.Perez-Mezcua, R. J.Jimenez Rioboó, M.Garcıa-Hernández, M.L.Calzada. Solution Synthesis of $BiFeO_3$ Thin Films onto Silicon Substrates with Ferroelectric, Magnetic, and Optical Functionalities, *J. Am. Ceram. Soc.*, **2013**, *96(10)*, 3061–3069.

4. A. Gómez-López. "Flexible ferroelectric BiFeO3 perovskite thin films processed by photo-chemical solution deposition". MSc, Facultad de Ciencias. Universidad Autónoma de Madrid, Spain. June 2021.

5. S.Krompiec, M.Krompiec, R.Penczek, H.Ignasiak. Double bond migration in N-alytic systems catalyzed by transition metal complexes. *Coord.Chem.Rev*., **2008**, *252*, 1819-1841.

6. K.Makino, A.Hagi, H.Ide, A.Murakami, M.Nishi. Mechanistic studies on the formation of aminoxyl radicals from 5,5-dimethyl-1-pyrroline-*N*-oxide in Fenton systems. Characterization of key precursors giving rise to background ESR signals. *Canadian Journal of Chemistry*, **1992**, *70(11)*, 2818-2827.

7. A.Bosnjakovic, S.Schlick. Spin Trapping by 5,5-Dimethylpyrroline-*N*-oxide in Fenton Media in the Presence of Nafion Perfluorinated Membranes: Limitations and Potential**.** *The Journal of Physical Chemistry B.* **2006**, *110* (22), 10720-10728.

8. J.M.Fontmorin, R.C.Burgos Castillo, W.Z.Tang, M.Sillanpää. Stability of 5,5-dimethyl-1-pyrroline-N-oxide as a spin-trap for quantification of hydroxyl radicals in processes based on Fenton reaction. *Water Research*, **2016**, 99, 24-32**.**